Journal of Power Sources 196 (2011) 5685–5696

Contents lists available at ScienceDirect

Journal of Power Sources

journal homepage: www.elsevier.com/locate/jpowsour

Reciprocating air flow for Li-ion battery thermal management to improve temperature uniformity

Rajib Mahamud, Chanwoo Park*

Department of Mechanical Engineering, University of Nevada, 1664 N. Virginia Street, Reno, NV 89557-0312, USA

ARTICLE INFO

Article history:
Received 13 January 2011
Received in revised form 14 February 2011
Accepted 17 February 2011
Available online 26 February 2011

Keywords:
Li-ion battery
Thermal management
Reciprocating flow
Electrical vehicle
CFD
Lumped-capacitance thermal model

ABSTRACT

The thermal management of traction battery systems for electrical-drive vehicles directly affects vehicle dynamic performance, long-term durability and cost of the battery systems. In this paper, a new battery thermal management method using a reciprocating air flow for cylindrical Li-ion ($LiMn_2O_4$/C) cells was numerically analyzed using (i) a two-dimensional computational fluid dynamics (CFD) model and (ii) a lumped-capacitance thermal model for battery cells and a flow network model. The battery heat generation was approximated by uniform volumetric joule and reversible (entropic) losses. The results of the CFD model were validated with the experimental results of in-line tube-bank systems which approximates the battery cell arrangement considered for this study. The numerical results showed that the reciprocating flow can reduce the cell temperature difference of the battery system by about 4 °C (72% reduction) and the maximum cell temperature by 1.5 °C for a reciprocation period of $\tau = 120$ s as compared with the uni-directional flow case ($\tau = \infty$). Such temperature improvement attributes to the heat redistribution and disturbance of the boundary layers on the formed on the cells due to the periodic flow reversal.

© 2011 Elsevier B.V. All rights reserved.

1. Introduction

Electric vehicles (EVs) and hybrid electric vehicles (HEVs) are considered to be sustainable and environmentally friendly transportation options in the midst of rising oil prices and global climate changes due to greenhouse gas emission. The traction battery systems for the electrical-drive vehicles houses a large number (hundreds to thousands) of high energy-density rechargeable batteries such as Li-ion, and Ni-MH to satisfy the demanding vehicle power requirements. The battery system performance greatly affects all the vehicle dynamic and electric parameters such as acceleration, regenerative braking and battery charging/discharging.

The battery thermal management (including both cooling and heating) is essential for electrical-drive vehicles to maintain proper cell temperature conditions in all weather conditions. The thermal imbalance among the cells significantly affects short and long-term performances of the vehicle battery systems. According to the Arrhenius law of battery electrochemistry, the battery reaction increases exponentially with the battery cell temperature. As a result, hotter cells degrade more quickly than colder cells [1–4] and those few overheated cells result in shortening the lifetime of a whole battery pack. The lifespan of the Li-ion cell, for example, is reduced by about two months for every degree of temperature rise in an operating temperature range of 30–40 °C [5]. The Li-ion battery system is required to maintain the maximum cell temperature below 40 °C and the cell temperature difference below 5 °C for a full lifespan [2].

The primary objectives of the battery thermal management are (1) to limit the battery cell temperatures below the allowed maximum cell temperature, $T_{s,\max}$; (2) to minimize the cell temperature difference, ΔT_s; and (3) to maintain the cell temperatures within the operating range for optimum performance and longevity of the battery system. Air (ambient and/or air-conditioned) has been the coolant of choice because of reliable and simple battery cooling systems. Specially, the battery cooling would be very challenging in the summer (ambient air temperature of 50 °C) without using vehicle air-conditioning system. The conventional battery cooling systems utilize the one-directional air flow moving from the inlet and outlet of the battery cooling systems. As a result of the convective heat transfer along the air stream, the air temperature at the outlet is always higher than the inlet and the downstream cells near to the outlet are likely hotter than the upstream cells. Most of the conventional battery thermal management systems actually use flow distributors (baffle), which also serve as battery holder, to create a strong convective heat transfer condition for the downstream cells in an attempt to compensate the unfavorable air temperature for the convective heat transfer [3].

* Corresponding author. Tel.: +1 775 682 6301; fax: +1 775 784 1701.
E-mail address: chanwoo@unr.edu (C. Park).

0378-7753/$ – see front matter © 2011 Elsevier B.V. All rights reserved.
doi:10.1016/j.jpowsour.2011.02.076

Nomenclature

A	area [mm^2]
Bi	Biot number
C	correction factor
c_p	specific heat capacity [J kg^{-1} K^{-1}]
D	diameter of a battery cell [mm]
dE_{oc}/dt	entropic coefficient [mV K^{-1}]
E	cell potential [V]
f	friction factor
h	convective heat transfer coefficient [W m^{-2} K^{-1}]
I	electrical current [A]
k	thermal conductivity [W m^{-1} K^{-1}]
L	length of a battery cell or characteristic length [mm]
l	duct length [mm]
$\dot{M}_f$	mass flow rate [kg s^{-1}]
n	total number of tubes (battery cells) or index number of the last tube (or battery cell)
NTU	number of transfer unit
Nu_D	Nusselt number based on the cell diameter D
$\mathrm{Nu}_{D,c}$	corrected Nusselt number
Pr	Prandtl number
p	pressure [Pa]
Q	heat transfer rate [W]
R	thermal resistance [K W^{-1}]
Re	Reynolds number
R_e	internal electrical resistance of a battery cell [mΩ]
S	spacing between cells [mm]
S_r	battery heat generation [W]
T	temperature [K]
$\overline{T}$	time-averaged temperature [K], $\bar{T} = \int T\,dt / \int dt$
t	time [s]
U	velocity [m s^{-1}]
V	volume [m^3]
$\dot{V}$	volumetric flow rate [m^3 s^{-1}]
w	width of the computational domain [mm]

Greek

$\overline{\Delta T}$	time-averaged temperature difference [K], $\overline{\Delta T} = \overline{T_{s,\max}} - \overline{T_{s,\min}}$
ε	porosity
μ	viscosity [Pa s]
ρ	density [kg m^{-3}]
τ	reciprocation period [s]

Subscripts

b	battery
c	cyclic or characteristic or correction
D	diameter
e	electrical
f	fluid phase
i	battery node index or duct inlet
irr	irreversible
ku	surface convection
L	longitudinal direction or duct outlet
LMTD	log mean temperature difference
max	maximum
min	minimum
n	index number for the last battery cell
oc	open circuit
o	duct outlet
p	pressure or particle
r	battery reaction
rev	reversible
s	solid phase or surface
T	transverse direction
u	convection
w	wall

Other symbols

–	time-averaged
∞	ambient condition or infinity
+	infinitely small incremental

In this study, the reciprocating flow created by a periodic reversal of the air flow was investigated in an effort to mitigate the inherent temperature gradient problem of the conventional battery system using the uni-directional coolant flow [1,6]. The reciprocating flow has been used for super-adiabatic combustion and heat recovery applications [7–10]. The reciprocating cooling flow can be created by using flip door valves and the unique duct design as shown in Fig. 1 as an example using the conventional uni-directional air blower. The reversible blower could be also used to generate the reciprocating flow using the existing duct system for the uni-directional flow system.

This paper presents the numerical results from both (i) a two-dimensional computational fluid dynamics (CFD) model created by the commercial software, ANSYS FLUENT, and (ii) a lumped-capacitance thermal model of battery cells and a flow network model. The battery heat generation was approximated by uniform volumetric joule and reversible (entropic) losses in battery cells [2,11–15]. The accuracy of the results of the CFD models was validated using the experimental data of friction coefficients and

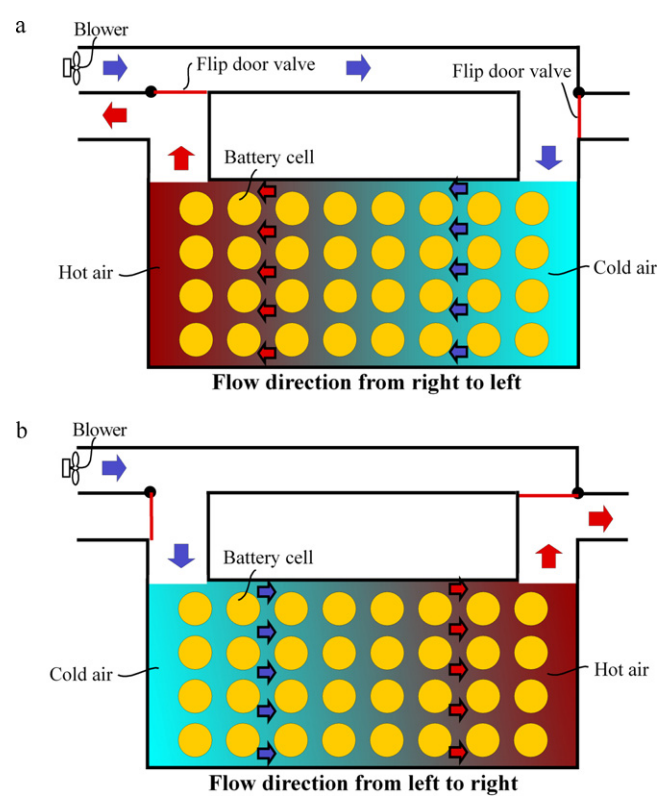

Fig. 1. Schematic view of a battery system using a reciprocating air flow for battery thermal management. The flow directions are (a) from right to left side and (b) from left to right side.

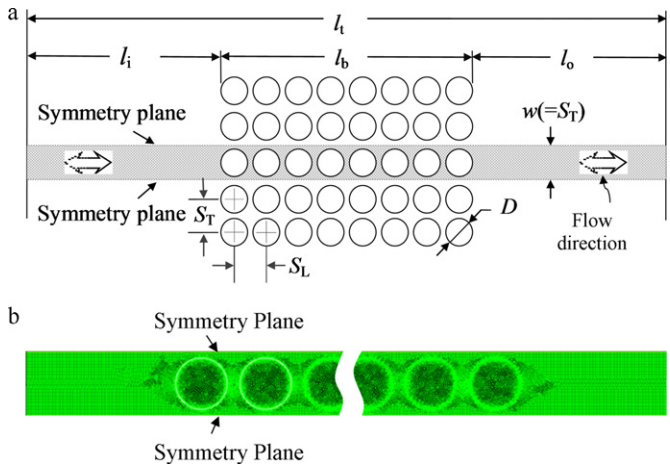

Fig. 2. (a) Battery system in in-line cell arrangement showing the computational domain (shaded region) of a representative battery submodule with eight cells considered for the numerical analysis and (b) the mesh system of the battery submodule.

heat transfer coefficients for the in-line tube-bank systems [16–21] which approximate the battery system considered for this study. A parametric study using various operating and design variables such as reciprocation period, cell spacing, coolant flow rate and different battery loading was carried out and the results are discussed in the following section.

2. Numerical computation methodology

2.1. Computational domain of the battery system

The cylindrical Li-ion ($LiMn_2O_4$/C, capacity: 3.6 Ah, $D \times L$ = 42.4 mm × 97.7 mm) cell was considered for this study. Two methods were used for the numerical analysis: (i) two-dimensional CFD model which provides precise results as the benchmark solutions but at the cost of an intensive computation (8–24 h per case); (ii) lumped-capacitance thermal model for battery cells and flow network model assuming each battery cell to have a uniform temperature and the air flow over the in-line cells at constant surface temperatures which provides reasonably accurate results on a light computation (15 min per case). The battery system considered for this study consists of multi rows (submodules) of a set of battery cells as shown in Figs. 1 and 2(a). The shaded region of the eight-cell submodule as shown in Fig. 2(a) was used as the computation domain for the numerical analysis. The symmetric planes were chosen between the battery submodules instead of the centerline of the battery submodule. This is because Karman vortexes are created behind the last cells at high Reynolds number conditions causing an asymmetrical flow. The computation domain also includes an extra flow region extended from the battery area to avoid developing velocity conditions affecting the computation results. The total length (l_t) of the computational domain of the battery system in the streamwise direction is 1060 mm including the portion of the battery cells (l_b = 413.4 mm). The length of the extension to the left side of the battery area is l_i = 323.3 mm and the length of the extension to the right side is l_o = 323.3 mm. The width (w) of the battery submodule is 53 mm. The battery diameter D is 42.4 mm. The dimensions and specifications of the battery system considered for this study are listed in Table 1. Only radial conduction in the battery cells was considered for this study because of the layered-film construction of cylindrical battery cells [22]. For example, the conduction thermal resistance in the radial direction of a spirally wound Li/$SOCl_2$ cell would be twenty times higher than the axial direction [23].

2.2. Two-dimensional CFD model

The two-dimensional CFD model was developed by using a commercial package, ANSYS FLUENT 12.1.4 [24] which is based on the finite volume method [25]. For the CFD analysis, the buoyancy effect was neglected; the Reynolds stress and renormalization group (k–ε) was used for the turbulent model; the Navier–Stokes momentum equation was solved by using second-order upstream difference scheme; the PISO (pressure-implicit with splitting of operators) algorithm for the unsteady problem and the PRESTO (pressure staggering option) for the swirling flow were considered. The reciprocating flow was created by using a journal file available from the FLUENT to periodically interchange the boundary conditions between the inlet and outlet, where a velocity boundary condition was used for the inlet and a pressure boundary condition was used for the outlet every reciprocation period.

The shaded region of the eight-cell submodule as shown in Fig. 2(a) was used as the computation domain for the CFD analysis. The mesh systems were generated by using commercial meshing software, GAMBIT [26]. The computational domain was meshed using structured quadrilateral cells of high skewness using a size function to assign finer meshes along the battery surface. The mesh quality was evaluated by checking the dependency of the results of the CFD analysis such as pressure drop of the coolant flow and maximum cell temperature on various mesh sizes. Finer mesh was used for the flow region, especially around the battery cells, whereas coarse mesh was used inside the battery cell volume. Considering the accuracy of the results and computation time, a mesh system consisting of 113,470 mesh elements for the baseline system as shown in Fig. 2(b) was chosen for the CFD analysis. The green lines in the figure represent the mesh lines which were too fine to clearly display. (For interpretation of the references to color in this text, the reader is referred to the web version of this article.)

The computational parameters such as time step and number of iteration per time step used for the analysis were chosen to ensure that the CFD results are independent on the computational parameters. The convergence criteria of the residuals of the computational variables are 10^{-4} for continuity and momentum equations and 10^{-6} for energy equation. Note that the reciprocating flow system is intrinsically unsteady problem but has a quasi-steady solution which is characterized by a cyclic oscillation every reciprocating period. The computational time was typically about 8–24 h to get a quasi-steady state solution using a Window NT workstation (64 bit OS) with an Intel Xeon Quad-Core processor (3.16 GHz) with 24 GB RAM.

2.3. Lumped-capacitance thermal model and flow network model

Commercial Li-ion batteries are typically constructed in a multilayer structure in which the radial thermal conductivity is lower than the axial one. Nevertheless, the thermal resistance by the radial conduction is still much less than the convective thermal resistance as air is used as the coolant (i.e., $Bi = L_c h_f / k_s < 0.1$). Therefore, a lumped-capacitance thermal model for battery cells assuming a uniform temperature in each cell might be sufficient without compromising accuracy of the numerical analysis [1–3]. The lumped-capacitance model, if properly validated, could provide an effective and simple computational tool to perform dynamic thermal analyses using battery duty cycles and real-time battery control on light and fast computation. In case of analyzing complex battery systems including duct, battery holder, flow baffle and electrical connector/wire, the CFD modeling would be the choice but require an immense effort on meshing, and computation as compared to the lumped-capacitance modeling.

The battery submodule of eight cells (shaded region in Fig. 2(a)) was considered for the numerical analysis using the lumped-

Table 1
Dimensions of battery cell and submodule and the baseline conditions used for the numerical analysis and thermophysical properties of Li-ion battery and air.

Battery technology: Li-ion battery (cathode: $LiMn_2O_4$, anode: carbon)			
Battery cell specification		Air properties (at 300 K)	
Capacity [Ah]	3.6	ρ_f [kg m^{-3}]	1.1614
D [mm]	42.4	k_f [W m^{-1} K^{-1}]	0.0263
L [mm]	97.7	$c_{p,f}$ [J kg^{-1} K^{-1}]	1007
M [kg]	0.3	μ_f [kg m^{-1} s^{-1}]	1.846×10^{-5}
A_{ku} [mm^2]	13,014.0	Pr_f	0.707
V_s [mm^3]	137,948.2		
ρ_s [kg m^{-3}]	2007.7		
k_s [W m^{-1} K^{-1}]	32.2		
$c_{p,s}$ [J kg^{-1} K^{-1}]	837.4	Baseline conditions	
dE_{oc}/dT [mV K^{-1}]	−0.3	Charge/discharge rate [C]	7
Battery submodule specification		$T_{f,\infty}$ [°C]	20
Number of cell in flow direction, n	8	$Re_{D,max}$	13,300
l_i [mm]	323.3	$\dot{V}_f$ [CFM]	8.8
l_o [mm]	323.3	τ [s]	1200
l_b [mm]	413.4	S_T [mm]	53
l_t [mm]	1060	S_L [mm]	53

capacitance cell thermal model. The thermal circuit diagram of the submodule is shown in Fig. 3(b) and (c). The energy equation for a cell (index number i) can be given by

$$(\rho c_p \dot{V})_{s,i} \frac{dT_{s,i}}{dt} = S_{r,i} - Q_{ku,i} \quad (1)$$

Here $S_{r,i}$ is the heat generation of a battery cell. The battery heat generation is approximated by the sum of (i) Joule (irreversible) and (ii) entropic (reversible) heats and is given by

$$S_{r,i} = Q_{irr} + Q_{rev} \quad (2)$$

The first term (Q_{irr}) in the battery heat generation represents the Joule heating based on the battery internal electrical resistance R_e and is given by

$$Q_{irr} = I(E - E_{oc}) = I^2 R_e \quad (3)$$

where the battery electrical resistance was experimentally determined by averaging over a range of the state-of-charge (SOC) and is expressed in a function of the cell temperature by [2]

$$R_e = -0.0001\ T^3 + 0.0134\,T^2 - 0.5345\,T + 12.407 \quad (4)$$

where R_e is the internal electrical resistance [mΩ] of a Li-ion battery cell. T is the cell temperature [°C].

The second term (Q_{rev}) in the battery heat generation represents the reversible entropic loss [12] and is given as

$$Q_{rev} = -IT\frac{dE_{oc}}{dT} \quad (5)$$

where the entropy coefficient dE_{oc}/dT is a function of charge density, SOC and cell temperature. The SOC-averaged value of −0.3 [mV K^{-1}] was used for the entropic coefficient dE_{oc}/dT which was obtained from the results of the experimental measurement of two half-cells ($LiMn_2O_4$/Li and Li/C) [11–13]. For the SOC range (100–70%) considered for this study as shown in Fig. 6, the composition stoichiometry ranges are y = 0.442–0.590 for the positive electrode ($Li_yMn_2O_4$) and x = 0.676–0.511 for the negative electrode (Li_xC_6) [14,15]. The entropic coefficient of −0.3 [mV K^{-1}] was obtained by adding the averaged values of the dE_{oc}/dT of the two electrodes over the corresponding stoichiometry ranges [11]. It is worth mentioning that for hybrid electric vehicle application, the entropic loss is often neglected, because at high charge/discharge rates, the irreversible Joule heating becomes dominant than the reversible entropic heating [14]. The Joule heating quadratically increases with respect to electrical current, whereas the entropic loss linearly increases with respect to electrical current and can be either positive (exothermic) or negative (endothermic) depending

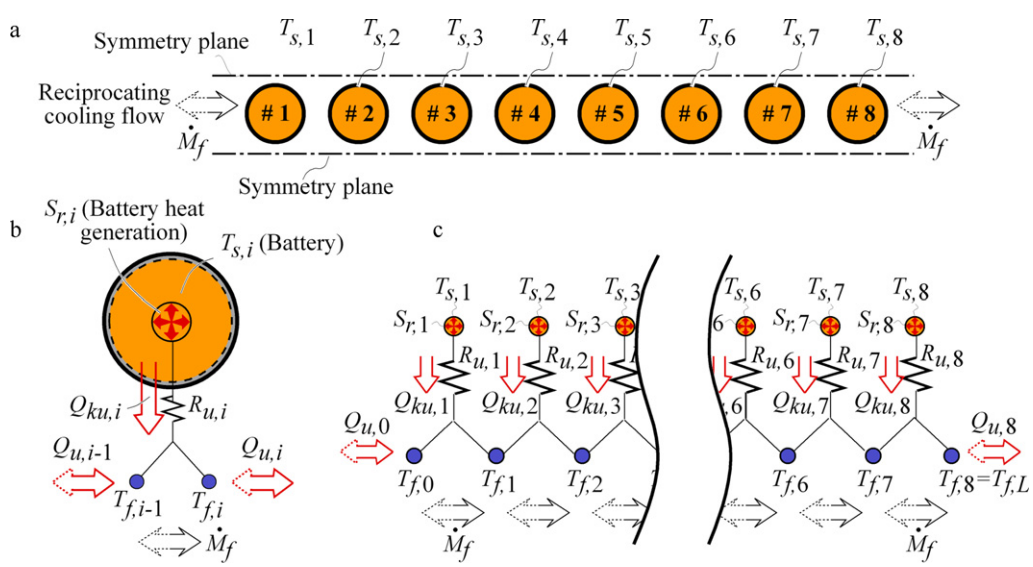

Fig. 3. (a) Battery submodule with eight cells used for the lumped-capacitance thermal modeling. (b) Thermal circuit diagram for a representative battery cell showing the battery heat generation and heat transfer. (c) Thermal network diagram for the battery submodule showing the temperature nodes for battery cells and fluid stream.

on the charging or discharging conditions. As a result, the net heating effect of the reversible heating could be negligible after a full cycle of charging/discharging.

As shown in Fig. 3(b) and (c), the surface convection heat transfer rates $Q_{ku,i}$ of a cell (i = 1, 2, . . ., 8 from the left and to the right side as shown in Fig. 3(c)) can be expressed using convection thermal resistances $R_{u,i}$ [10,21] and depending on the flow direction, are given by

$$Q_{ku,i}\begin{cases}\dfrac{T_{s,i}-T_{f,i-1}}{R_{u,i}} & \text{for the coolant flowing from the left to the right side (notated as solid arrows in Fig. 3(b) and (c))}\\ \dfrac{T_{s,i}-T_{f,i}}{R_{u,i}} & \text{for the coolant flowing from the right to the left side (notated as dotted arrows in Fig. 3(b) and (c))}\end{cases} \tag{6}$$

where the convection thermal resistances for the cells are given by

$$R_{u,i}=\frac{1}{(\rho c_p\dot{V})_f(1-e^{-\mathrm{NTU}})} \tag{7}$$

$$\mathrm{NTU}=\frac{A_{ku,i}h}{(\rho c_p\dot{V})_f}=\frac{A_{ku,i}}{(\rho c_p\dot{V})_f}\frac{\mathrm{Nu}_D k_f}{D} \tag{8}$$

where the Nusselt number (Nu_D) proposed by Zukauskas and Ulinskas [16,21] for the in-line tube-banks system is given by

$$Nu_D=\begin{cases}0.8Re_{D,\max}^{0.4}Pr^{0.36}(Pr/Pr_w)^{0.25} & 10^0<Re_{D,\max}<10^2\\ 0.51Re_{D,\max}^{0.5}Pr^{0.36}(Pr/Pr_w)^{0.25} & 10^2<Re_{D,\max}<10^3\\ 0.27Re_{D,\max}^{0.63}Pr^{0.36}(Pr/Pr_w)^{0.25} & 10^3<Re_{D,\max}<2\times10^5\\ 0.021Re_{D,\max}^{0.84}Pr^{0.4}(Pr/Pr_w)^{0.25} & 2\times10^5<Re_{D,\max}<2\times10^6\end{cases} \tag{9}$$

$$Re_{D,\max}=\frac{\rho U_{\max}D}{\mu} \tag{10}$$

$$U_{\max}=\frac{S_T}{S_T-D}U \tag{11}$$

Here U is the free space velocity. $U_{\max}$ is the maximum fluid velocity in the transverse spacing (S_T-D) between two vertically adjacent cells. The Nusselt number in Eq. (9) is valid only when the number of cells in the streamwise direction exceeds 20. For the eight-cell system used for this study, a correction factor C = 0.95 [21] is used as below

$$\mathrm{Nu}_{D,c}=C\,\mathrm{Nu}_D \tag{12}$$

The comparison of the empirical correlation (Eq. (9)) and the results from 2D CFD modeling is discussed in Section 3.

As shown in Fig. 3(b), the energy equation for the fluid stream flowing over a cell (i = 1, 2, . . ., 8) can be given by

$$Q_{u,i-1}-Q_{u,i}+Q_{ku,i}=0 \tag{13}$$

where

$$Q_{u,i-1}-Q_{u,i}=(\rho\,c_p\dot{V})_f(T_{f,i-1}-T_{f,i})=(\dot{M}c_p)_f(T_{f,i-1}-T_{f,i}) \tag{14}$$

The first-order ordinary differential equations (ODEs) for eight cells (Eq. (1)) were solved using an initial-value solver based on the backward differentiation formulas (BDF) method [27].

3. Results and discussion

3.1. Validation of CFD model using uni-directional flow system

The battery cell arrangement used for this study can be approximated by the in-line tube-bank system [16–21,28] as shown in Fig. 2. The 2D CFD model was validated using the experimental results of the tube-bank systems using a uni-directional flow. The experimental results used for the validation include the pressure drop (friction factor) [17,19] and heat transfer (Nusselt number) [16,20,21].

Fig. 4 shows the comparison of the friction factor results from the 2D CFD simulation and the experimental measurement of the in-line tube-bank systems under an isothermal condition. The friction factor (f) is defined by

$$f=\frac{\Delta p}{(1/2)n\rho U_{\max}^2} \tag{15}$$

where Δp is the total pressure drop of the tube-bank system. n is the total number of the tubes (or cells) in the streamwise direction. It is shown from Fig. 4 that there is a noticeable transition in the friction factor curves around the Reynolds number of 5×10^3 where the flow transition from laminar to turbulent regimes occurs. It is also shown that the result from the 2D CFD simulation is in good agreement (within 5% variation at the baseline Reynolds number $\mathrm{Re}_{D,\max}$ = 13300) with the experimental results despite the fact that the bounding walls could introduce a three-dimensional end effect into the experimental results.

The Nusselt number correlations from the experimental measurement of the inline-tube-bank systems [16,18–21] were also compared with the results from the 2D CFD simulation as shown in Fig. 5. Two empirical correlations of the Nusselt number were considered for the comparison for the model validation: one by Zukauskas and Ulinskas [Eqs. (9)–(11)] using the Reynolds number based on the maximum velocity ($U_{\max}$) in the least free space; the other by Whitaker [20] using the Reynolds number based on the free space velocity (U) and the particle diameter (D_p) as defined below.

$$Re_{D_p}=\frac{\rho UD_p}{\mu}\frac{1}{1-\varepsilon} \tag{16}$$

$$D_p=\frac{6V_p}{A_p}=\frac{3}{2}D \tag{17}$$

where ε is the porosity (or void volume ratio) of the portion (l_b as shown in Fig. 2(a)) of the battery system occupied by the battery cells.

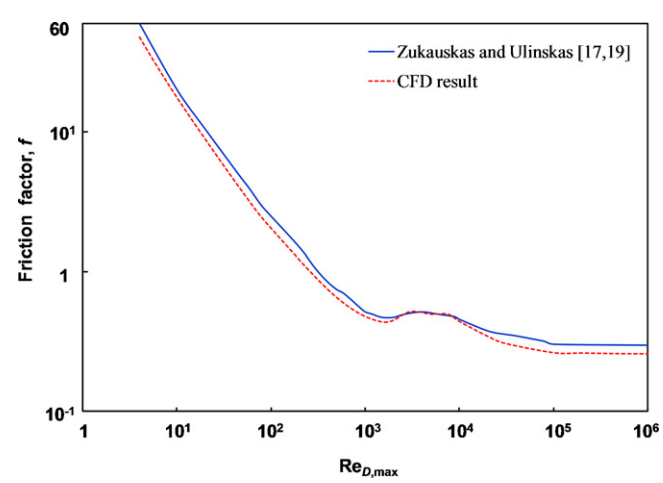

Fig. 4. Comparison of friction factor versus Reynolds number between the CFD results and experimental results of the in-line tube-bank system using isothermal wall condition and uni-directional flow.

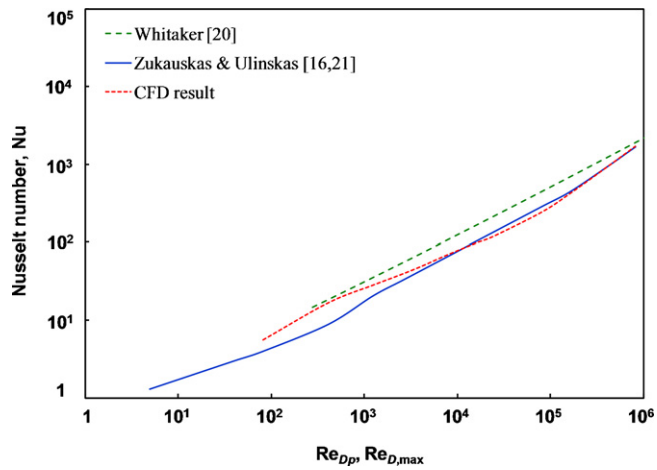

Fig. 5. Comparison of Nusselt number versus Reynolds number between the CFD results and experimental results of the in-line tube-bank system using isothermal wall condition and uni-directional flow.

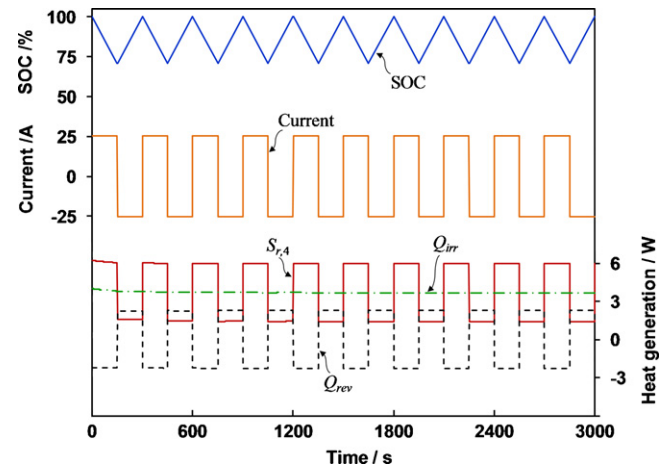

Fig. 6. Temporal variation of the heat generation rates (reversible, irreversible and total) for the battery cell #4 (refer to Fig. 3(a)), electrical current and state-of-charge (SOC) for the baseline condition.

The Nusselt number using the results of the CFD simulation is calculated using a log-mean temperature difference (LMTD) [21] and is given by

$$\mathrm{Nu}_D = \frac{hD}{k_f} \tag{18}$$

where

$$h = \frac{\dot{M}_f c_{p,f}(T_{f,L} - T_{f,0})}{A_s T_{\mathrm{LMTD}}} \tag{19}$$

$$A_s = n\pi DL \tag{20}$$

$$T_{\mathrm{LMTD}} = \frac{(T_{s,8} - T_{f,L}) - (T_{s,1} - T_{f,0})}{\ln((T_{s,8} - T_{f,L})/(T_{s,1} - T_{f,0}))} \tag{21}$$

Here D is the diameter of the battery cell. L is the length of the cell. n is the total number of the cells. $T_{s,1}$ and $T_{s,8}$ are the temperature of the first and eighth cells, respectively. $T_{f,0}$ and $T_{f,L}$ are the fluid temperatures at the left and right sides of the battery system, respectively (refer to Fig. 3(c)).

As shown in Fig. 5, the Nusselt number from the 2D CFD analysis is in good agreement (within 3.5% variation at the baseline Reynolds number $\mathrm{Re}_{D,\max} = 13{,}300$) with the experimental results of the in-line tube-bank system using the uni-directional flow [16,18–21]. Therefore, it is rational to conclude from the comparisons of the uni-directional flow system in Figs. 4 and 5 that the 2D CFD model is reasonably accurate to be used for the analysis using the reciprocating flow system.

3.2. Results of reciprocating flow system using baseline conditions

The operation conditions and design variables such as reciprocation period, cell spacing, different battery loading, and air flow rate were considered for the parametric study to investigate the effect of the variables on battery cooling performance, especially battery cell temperature. The dimensions and thermo-physical properties of the Li-ion battery cell and battery system used for this study are listed in Table 1. Few important baseline conditions used for the parametric study are listed below.

- *Battery technology:* Li-ion battery (cathode material: $LiMn_2O_4$, anode material: carbon; cell capacity = 3.6 Ah; diameter D = 42.4 mm and length L = 97.7 mm).
- *Battery duty cycle:* the constant stepwise charge and discharge of 7 C (25.2 A) with each half cycle period of 150 s were used. The battery duty cycle was chosen to maintain the SOC value higher than 70% (refer to Fig. 6).
- *Inlet air temperature:* $T_{f,\infty} = 20\,^{\circ}\mathrm{C}$. The air as the coolant fluid was assumed to be conditioned by vehicle air-conditioning system.
- *Reciprocation period:* $\tau = 1200$ s. The cyclic period (τ) of the reciprocating flow is defined as the time for a reciprocating flow to recover its initial flow direction. Note that the uni-directional flow with no change in flow direction is a special case of the reciprocating flow having an infinite reciprocation period ($\tau = \infty$).
- *Battery cell spacing:* $S_T/D = 1.25$ was used for the transverse direction and $S_L/D = 1.25$ was used for the longitudinal (streamwise) direction. Note that $S/D = 1.0$ means no gap between the cells (refer to Fig. 2(a)).
- *Air flow rate:* the volumetric flow rate $\dot{V}_f = 8.8$ CFM per a battery submodule of eight cells was used which is equivalent to the fluid velocity of 1 m s^{-1} or $\mathrm{Re}_{D,\max} = 13{,}300$.

Fig. 6 shows the profiles of the electrical current, SOC, and battery heat generation of the fourth cell (#4) chosen as a representative cell of the battery system (refer to Fig. 3). The battery heat generation considered for this study consists of irreversible (Joule) and reversible (entropic) parts as defined in Eq. (2). The irreversible part is always exothermic and dominant for higher current conditions. Whereas, the irreversible part can be either exothermic or endothermic, thus it could be canceled out after a full cycle of charging/discharging.

Fig. 7 shows the results of the temperature and flow velocity from the CFD analysis using the baseline conditions. Fig. 7(a) shows the temperature contour of the battery submodule at various times within the reciprocating period of $\tau = 1200$ s. The temperature results were obtained from the 6th cycle (t = 6000–7200 s) when a quasi steady-state was achieved. The quasi steady-state is defined as the state where the oscillation amplitudes of the cell temperatures converge to constant values. The quasi steady-state condition is more discussed in the next section. The direction of the reciprocating flow at the beginning of the 6th cycle $t_c(= t - 4\tau) = 0^+$ is from the right to the left side. Shortly after that moment (within few milliseconds), the flow direction is reversed, i.e., from the left to the right side and quickly becomes fully developed. At the end of the half cycle $t_c = \tau/2$, the flow direction is reversed again. At the end of the full cycle $t_c = \tau$, the temperature profile is recovered to the initial condition at $t_c = 0^+$. It is also observed from Fig. 7(a) that the temperatures of a pair of the outer cells located downstream of the flow (i.e., #1 and 2 at $t_c = 0^+$ and #7 and 8 at $t_c = \tau/2$) are close each other. From a close examination of the velocity results, it is

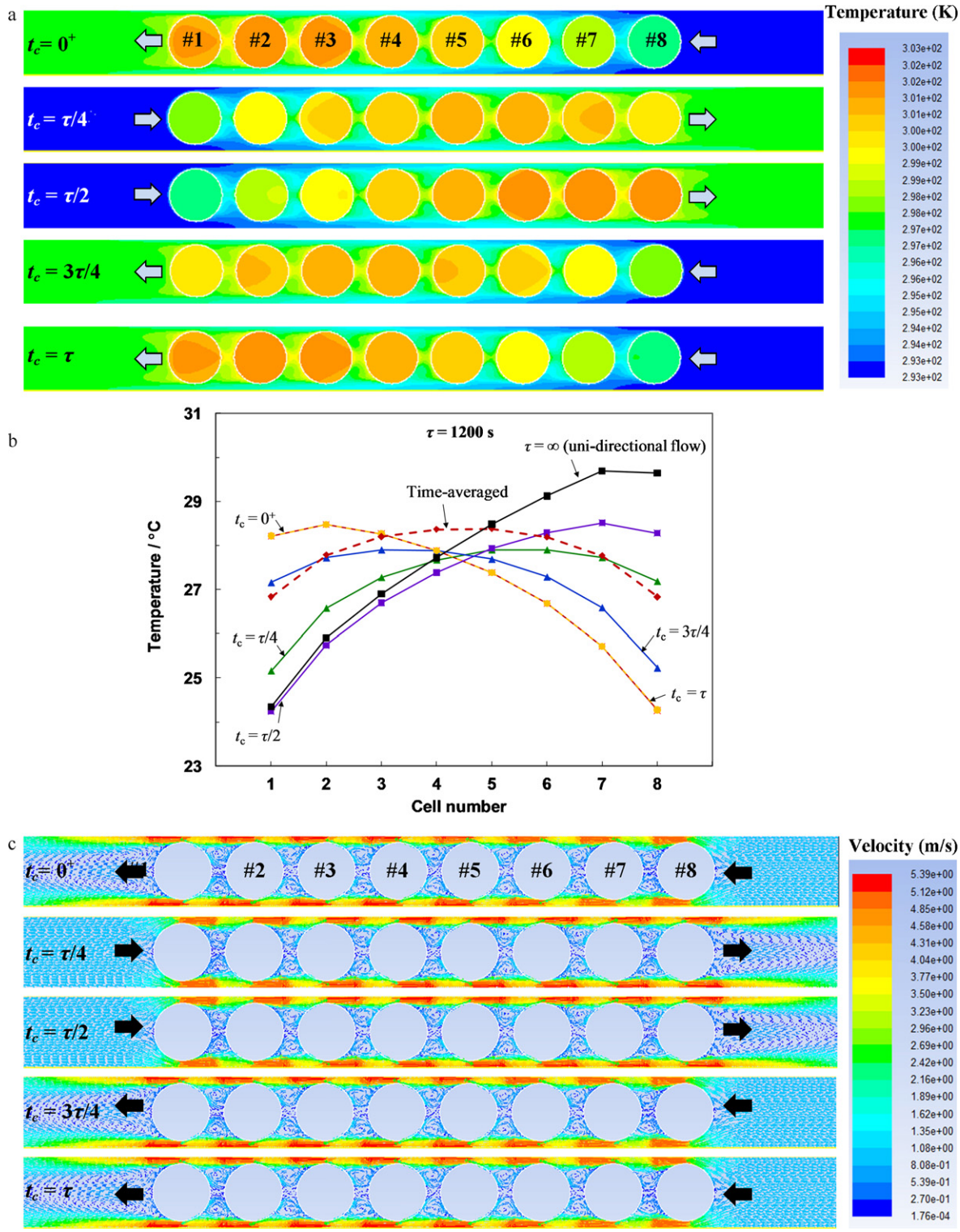

Fig. 7. Temporal progression of (a) temperature contours, (b) battery cell temperatures, and (c) velocity vector contours of the battery submodule under the baseline condition ($\tau = 1200$ s).

observed that it takes only few milliseconds for the old flow pattern to fade away and for the new flow pattern to fully establish when the flow direction is reversed.

Fig. 7(b) shows the temporal variation of the area-averaged temperature of each cell at various times. It is observed from the figure that the temperatures pivot at the center (between #4 and 5 cells) of the battery system. As a result, the temperatures of the inner cells vary less, while the outer cell temperatures oscillate more. The figure also shows that the maximum (both time-averaged and instantaneous) temperatures of the reciprocating flow are lower than the unidirectional case ($\tau = \infty$). Especially, the maximum difference of the time-averaged temperatures (notated in red dotted line) is 1.5 °C which is much lower than the uni-directional case of about 5.5 °C. It is worth noting that the instantaneous maximum temperature occurs at the second (#2) and seventh (#7) cells, while the time-averaged maximum temperature occurs at

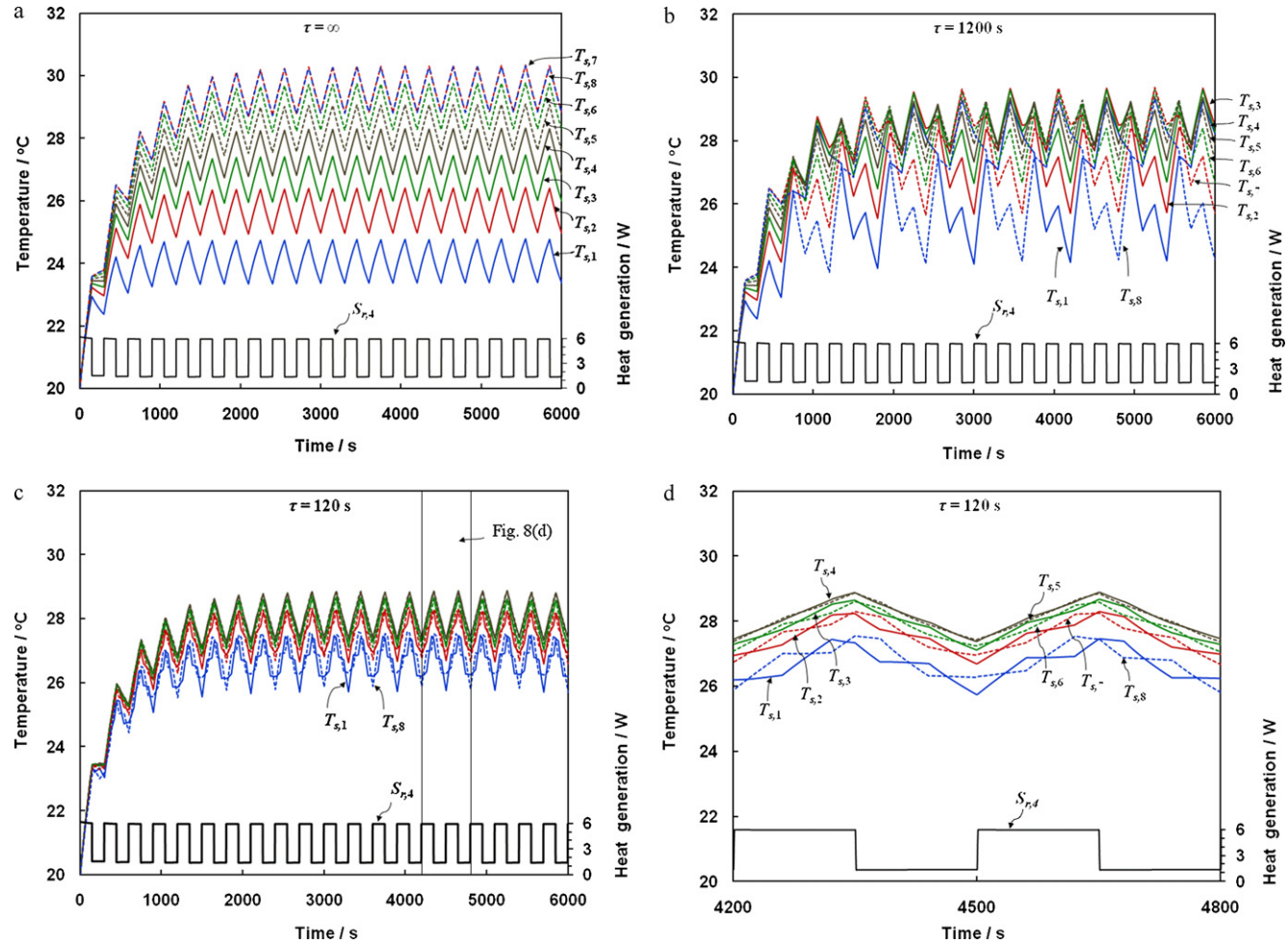

Fig. 8. Temporal variations of the battery cell temperatures for various reciprocation periods and the total battery heat generation of the battery cell #4 (refer to Fig. 3(a)): (a) $\tau = \infty$, (b) $\tau = 1200$ s, and (c) $\tau = 120$ s. (d) A magnified view of the quasi steady-state temperatures for the reciprocation periods of $\tau = 120$ s.

the cells (#4 and 5) near or at the middle of the battery system. The time-averaged maximum temperature is the maximum of the time-averaged temperature of the cells over a reciprocating period. The definition of the time-averaging of the cell temperatures is discussed in the next section.

Fig. 7(c) shows the velocity vector field at various times within the reciprocating period of $\tau = 1200$ s. In the figure, it is observed that the air flow accelerates and decelerates while passing through the least gap (the transverse spacing $S_T - D$) between the cells and the flow separations are created after each cell, except that rather large recirculation is created behind the last cell with respect to the flow direction. It is also observed that the stream through the transverse spacing is prevailing than one through the longitudinal spacing ($S_L - D$). This flow channeling effect is severer with narrower longitudinal spacing and is very detrimental for the battery cooling because of ineffective use of the battery surface for forced convective heat transfer, which could be mitigated by using a larger longitudinal spacing and flow deflectors.

3.3. Effect of reciprocation period

The temporal variations of the battery cell temperatures and heat transfer rates for various reciprocation periods are shown in Figs. 8 and 9. The temperature and heat transfer results were obtained from the 2D CFD model for three different reciprocating periods: $\tau = \infty$, 1200 and 120 s.

Figs. 8 and 9(a) show the results of the "uni-directional flow case" which is a special case of the reciprocating flow with $\tau = \infty$ as the coolant constantly flows from the left to the right side. In Figs. 8 and 9(a), a periodic fluctuation of the temperature and heat transfer rate is shown due to the alternating sign of the entropic heat (Q_{rev}) depending on charging/discharging of the battery cycle with a period of 150 s as shown in Fig. 6. However, the temperatures and heat transfer rates quickly converge and approach to quasi steady-states around 5000 s as shown in Figs. 8 and 9(a). The time-averaged temperatures were calculated after reaching the quasi steady-state over a period (300 s) of the battery duty cycle. Note that since the heat generation is not constant due to the sign-alternating entropic heat, the maximum temperature and average maximum temperature are different for the uni-directional flow case as shown in Fig. 10.

It is also observed from Fig. 8(a) that the lowest temperature occurs at the first cell (#1) and the highest temperature occurs at the seventh cell (#7) and the maximum cell temperature difference ($\Delta T_{s,\max}$) is 5.5 °C for the uni-directional flow case. Although the highest cell temperature is expected to occur at the last cell (#8) near to the flow exit due to the highest air temperature, the highest cell temperature occurs at the seventh cell (#7). This is because the eighth cell is exposed to more convective environment due to bigger recirculation formed behind the cell as shown in Fig. 7(c) than the inner cells. It is worth mentioning that the lumped thermal model using the empirical correlations (Eqs. (1)–(8)) always predicts the highest temperature in the last cell (#8) which attributes

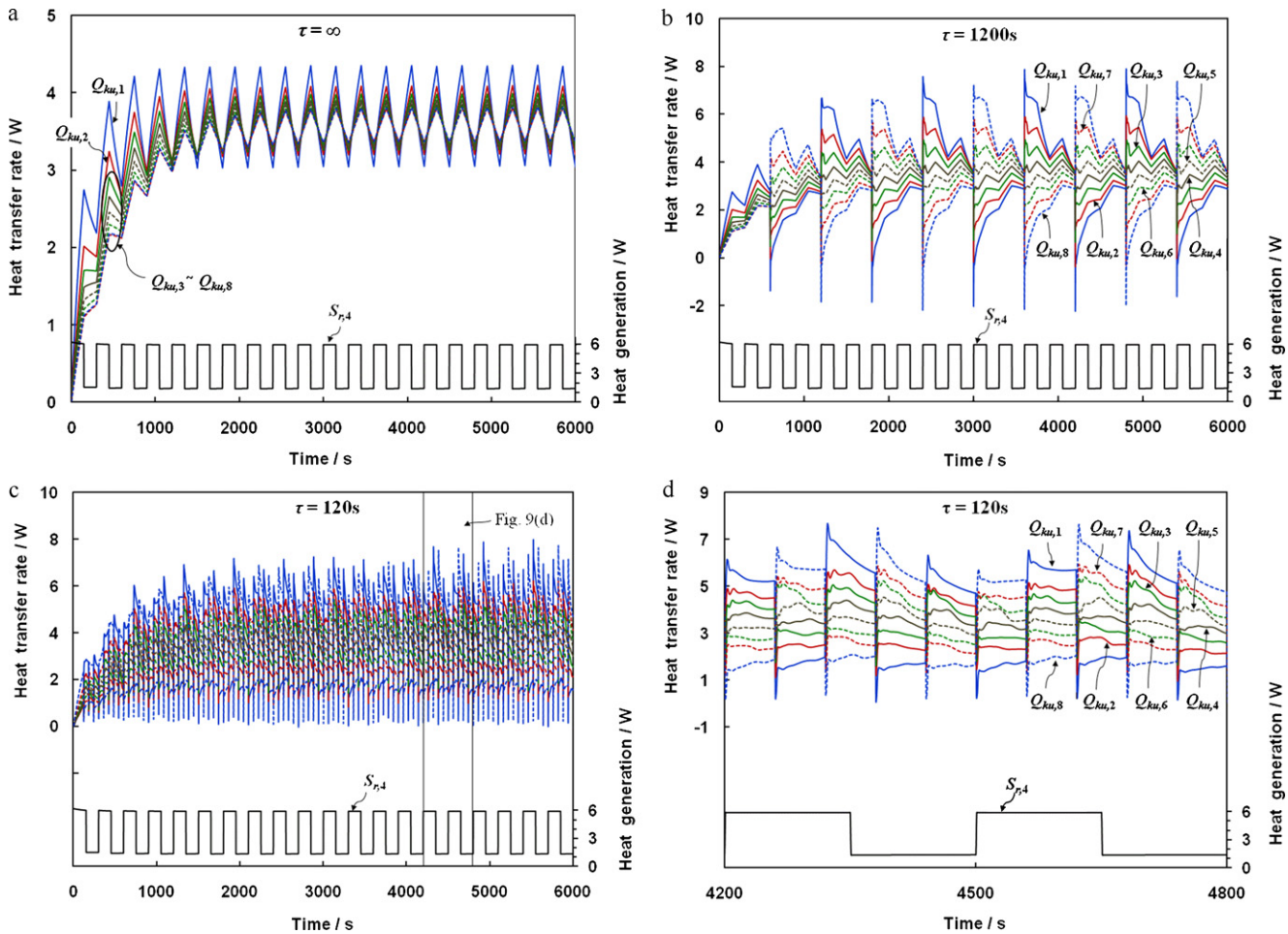

Fig. 9. Temporal variations of the heat transfer rates for various reciprocation periods and the total battery heat generation of the battery cell #4 (refer to Fig. 3(a)): (a) $\tau = \infty$, (b) $\tau = 1200$ s, and (c) $\tau = 120$ s. (d) A magnified view of the quasi steady-state heat transfer rates for the reciprocation periods of $\tau = 120$ s.

to the fact that the empirical correlations predicts the averaged heat transfer for the cells in the system.

For the "reciprocating flow cases" as shown in Figs. 8(b)–(d) and 9(b)–(d), the coolant flow direction is reversed at every half cycle ($t_c = \tau/2$) of each reciprocating period. Fig. 8(b) and (c) shows the cell temperatures and the total battery heat generation of the fourth cell (#4) for two different reciprocating periods of $\tau = 1200$ and 120 s. Fig. 9(b) and (c) shows the convective heat transfer rates of the cells and the total battery heat generation of the fourth cell (#4) for the corresponding reciprocating periods. Figs. 8(d) and 9(d) show the magnified view of the inset boxes shown in Figs. 8(c) and 9(c).

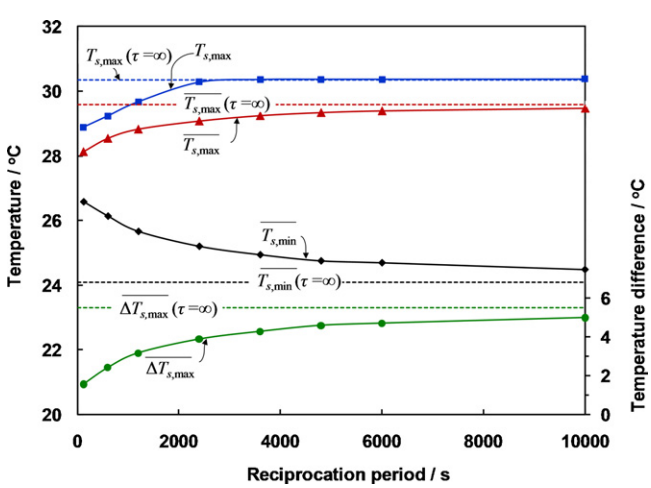

Fig. 10. Effect of the reciprocation period on the cell temperatures (instantaneous maximum; time-averaged maximum and minimum and differential).

Fig. 8(b) shows that the temperatures of the outer cells (#1 and #8) near to the flow inlet and outlet have a bigger swing than the inner cells due to the larger change in the ambient temperature and strong convective heat transfer by the jet impingement of the approaching flow which is also shown in Fig. 9(b). The symmetric oscillatory behavior of the cell temperatures as shown in Fig. 7(b) happens for all reciprocating periods. It is observed that the larger the reciprocating period is, the bigger the swings in the cell temperatures and convective heat transfer rates are. This is because of the longer time for the cell temperature to change resulting in the larger temperature difference between the cells and air temperature. Note that regardless of the reciprocating period, the amplitudes of the temperature swing tends to converge to quasi steady-states around 5000 s, similarly found in the uni-directional case.

For relatively shorter reciprocating periods ($\tau = 120$ s) as shown in Fig. 8(c) and (d), the temperatures of the inner cells are always higher than the outer cells. This is due to the heat accumulation effect by the fast reversal of the reciprocating flow. From the practical viewpoint of battery cooling system operation, smaller period would be not desirable for actual applications.

Fig. 10 shows the variation of the time-averaged temperatures with the reciprocation period, which were calculated over a full reciprocating period after the quasi steady-state is achieved. The

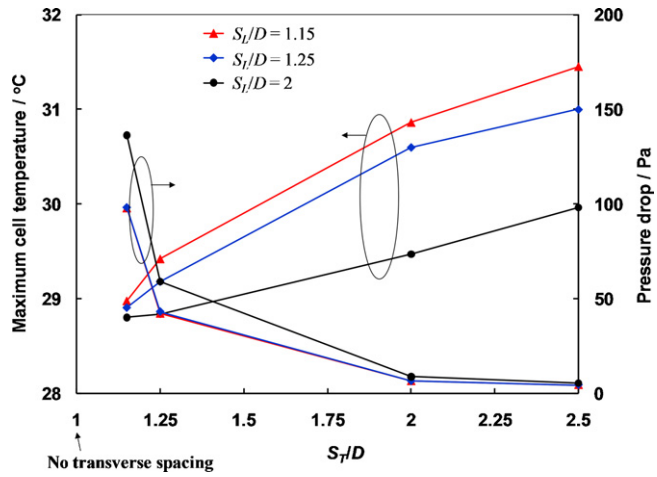

Fig. 11. Effect of the battery spacing on the maximum cell temperature and pressure drop.

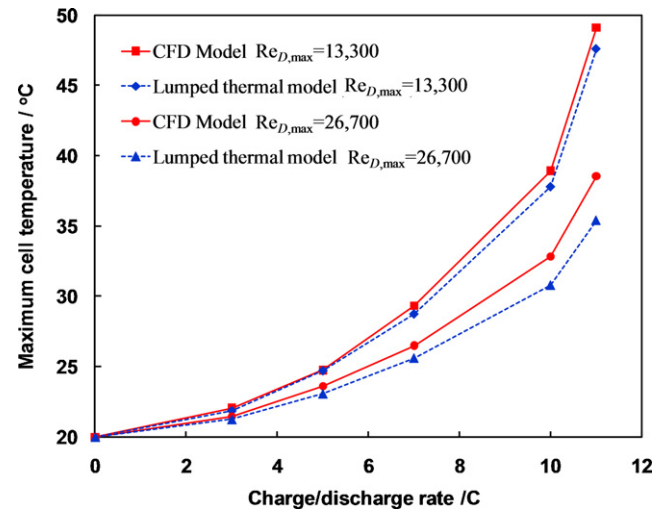

Fig. 12. Effect of the battery loading and air flow rate on the maximum cell temperature.

maximum ($\overline{T_{s,\max}}$) and minimum ($\overline{T_{s,\min}}$) time-averaged temperatures are defined by

$$\overline{T_{s,\max}} = \int_0^{\tau} \frac{T_{s,\max}\ dt}{\tau} \tag{22}$$

$$\overline{T_{s,\min}} = \int_0^{\tau} \frac{T_{s,\min}\ dt}{\tau} \tag{23}$$

where $\overline{T_{s,\max}}$ could indicate the level of the thermal stress (or health) of a battery system. The difference between the maximum and minimum of the time-averaged cell temperatures is given by

$$\overline{\Delta T_{s,\max}} = \frac{\int_0^{\tau}(T_{s,\max} - T_{s,\min})\ dt}{\tau} = \overline{T_{s,\max}} - \overline{T_{s,\min}} \tag{24}$$

$\overline{\Delta T_{s,\max}}$ is related to the level of the imbalance of the thermal stress of a battery system.

It is shown in Fig. 10 that as the reciprocating period decreases $\overline{T_{s,\max}}$ decreases and $\overline{T_{s,\min}}$ increases, thus $\overline{\Delta T_{s,\max}}$ decreases (i.e., more uniform temperature). Note that the instantaneous maximum cell temperature $T_{s,\max}$ is always higher than the time-averaged one $\overline{T_{s,\max}}$. It is true for the uni-directional case ($\tau = \infty$) because of the temperature swing due to the sign-alternating entropic heat. It is also shown in Fig. 10 that the maximum of the time-averaged temperatures $\overline{T_{s,\max}}$ for the reciprocating flow case of $\tau = 120$ s is 28.1 °C while $\overline{T_{s,\max}} = 29.6$ °C for the uni-directional flow ($\tau = \infty$). $\overline{\Delta T_{s,\max}}$ for the reciprocating flow of $\tau = 120$ s is significantly reduced to 1.5 °C from $\overline{\Delta T_{s,\max}} = 5.5$ °C for the uni-directional flow case.

3.4. Effect of battery cell spacing

The cell spacing is defined in both horizontal (longitudinal spacing S_L) and vertical directions (transverse spacing S_T) as shown in Fig. 2(a). Fig. 11 shows the effect of the cell spacing on the maximum cell temperature of the battery system under the baseline conditions. The maximum cell temperature is the instantaneous value of the maximum cell temperature in the battery system at any given time. As shown in Fig. 7(b), the maximum cell temperature always occurs at the second (#2) and seventh (#7) cells at the time of the flow reversal ($t_c = 0$ or $\tau/2$) because of the increased heat transfer of the most outer cells (#1 and #8) due to the large flow recirculation behind them.

It is observed from Fig. 11 that as the transverse spacing (S_T) decreases, the cell temperature are decreased because the flow velocity is increased due to the decreased flow area resulting in increased convective heat transfer and pressure drop. It is also observed from the figure that longitudinal spacing (S_L) gets larger, the maximum cell temperature is decreased, this is because the flow creates bigger eddies in the longitudinal spacing of the cells rather than just passing over the cells (flow channeling) as shown in Fig. 7(c). As a result, the pressure drop of the system is increased. Therefore, it is summarized that the cell temperature is decreased with larger longitudinal and smaller transverse spacing and vice versa for the pressure drop. This competing result suggests the existence of the optimum spacing for the lowest maximum cell temperature for a fixed pumping power consumption of the air flow. The flow channeling as previously discussed in Fig. 7 could be mitigated by using a flow baffle which is commonly used to redirect the flow in commercial battery systems. Note that smaller spacing would be preferred because of the packaging constraints of the battery systems in vehicles.

3.5. Effect of different battery loading

Fig. 12 shows the effect of the battery charge/discharge rate on the instantaneous maximum cell temperature under the baseline conditions. For this calculation, the battery charge/discharge in the stepwise profile as shown in Fig. 6 was used by varying only the magnitude of the electrical current. The battery heat generation was calculated by the sum of Joule (irreversible) and entropic (reversible) heats as given in Eq. (5). The reversible entropic heating has a linear dependence with the electrical current, thus the net heating effect is zero during a full cycle of the charging/discharging. The irreversible Joule heating is, however, always positive because of the quadratic dependence with the current and becomes more dominant in the battery heat generation at higher charging/discharging rates. As shown in Fig. 12, the maximum cell temperature increases quadratically with the charge/discharge rate because of the non-zero Joule heating effect during the current cycling.

Fig. 12 also shows the effect of the air flow rate on the instantaneous maximum cell temperature. The instantaneous maximum temperature always occurs at the second cell (#2) or at the seventh cell (#7) of the battery system depending on the flow direction as previously discussed with Fig. 7. It is observed from Fig. 12 that the lower air flow rate ($Re_{D,\max} = 13{,}300$) is insufficient to limit the cell temperature below 40 °C at the high loading condition (>10 C). Fig. 12 also shows the comparison of the instantaneous maxi-

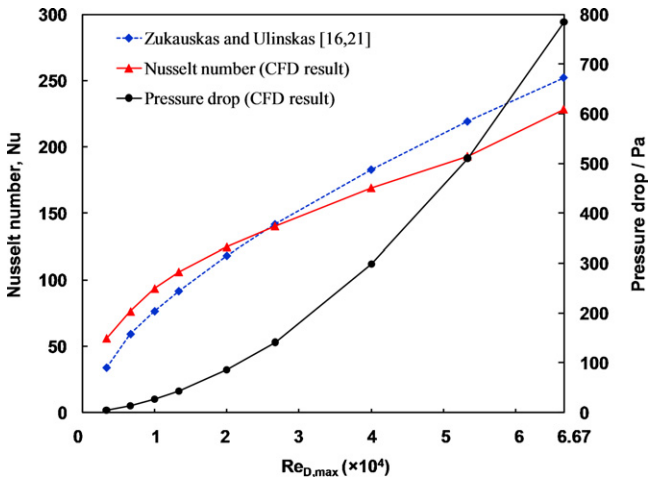

Fig. 13. Effect of the air flow rate on the Nusselt number and pressure drop.

mum temperatures from the CFD model and a lumped-capacitance model. The results from the CFD and lumped thermal models were well matched, especially for the lower Reynolds number ($Re_{D,max}$ = 13,300).

3.6. Effect of air flow rate

As the air flow rate is increased, the convective heat transfer on the cells is expected to be increased, thus the cell temperatures are decreased but at the expense of higher pressure drop (or pumping power). Figs. 13 and 14 show the effect of the air flow rate on the heat transfer and instantaneous maximum cell temperature, respectively. Because of the transient nature of the cell temperatures due to the reciprocating flow, the log-mean temperature difference using the time-averaged cell temperatures over a full cycle of the reciprocating flow was used for the calculation of the Nusselt number in Fig. 13 (refer to Eq. (22)).

Fig. 13 shows that the Nusselt number increases more rapidly until $Re_{D,max}$ = 13,300 where the transition between the laminar and turbulent regimes occurs (also refer to Fig. 4). In Fig. 13, the Nusselt number of the CFD model for the reciprocating flow cases was also compared with the empirical correlation [Eq. (9)] developed for the uni-directional flow system [16,19,21]. As shown in Fig. 13, for the Reynolds numbers below $Re_{D,max}$ = 26,600, the Nusselt number of the CFD model is greater than the empirical correlation and vice versa for the Reynolds numbers above $Re_{D,max}$ = 26,600. Note that the similar result is also shown in Fig. 5. Fig. 13 also shows that the pressure drop rapidly increases quadratically with the Reynolds number.

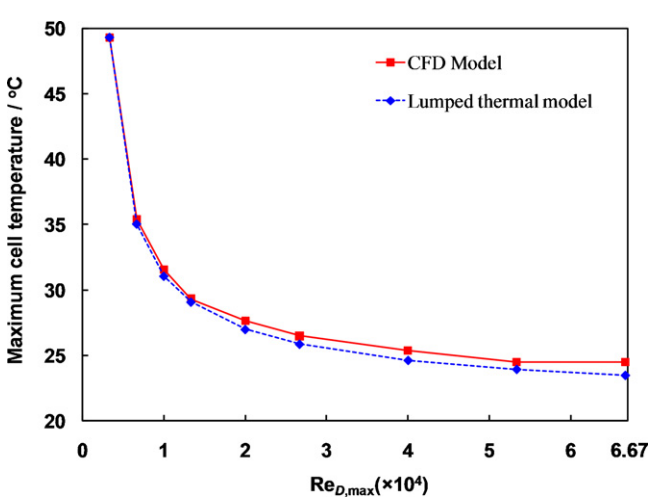

Fig. 14. Effect of the air flow rate on the maximum cell temperature.

Fig. 14 shows the change of the instantaneous maximum cell temperature as the Reynolds number is increased. As shown in the figure, the maximum cell temperature is quickly decreased until $Re_{D,max}$ = 13,300 where the slope change of the Nusselt number happens due to flow transition as shown in Fig. 13. After the Reynolds number, the cell temperature rather slowly decreases as the air flow rate increases. The optimum conditions for higher heat transfer and lower pressure drop (or pumping power) could exist. The figure also shows the comparison of the temperatures of the 2D CFD and lumped thermal models. The maximum cell temperature from the lumped thermal model is always lower than the CFD model. This attributes to the fact that the empirical correlation used for the lumped thermal model will predict the averaged heat transfer for the entire cells. It is concluded from Figs. 13 and 14 that the heat transfer correlations for the uni-directional flow systems is reasonably accurate enough to be used for the reciprocating flow systems. If a proper heat transfer correlation is available, the lumped-capacitance thermal model would be very suitable for real-time battery thermal analyses requiring time-efficient and fast computation.

4. Conclusion

A reciprocating air flow was used for battery thermal management of electrical-drive vehicles to improve temperature uniformity, and reduce maximum cell temperature. The reciprocating flow for the battery thermal management of cylindrical Li-ion ($LiMn_2O_4$/C) cells was numerically analyzed using (i) a two-dimensional CFD (computational fluid dynamics) model and (ii) a lumped-capacitance thermal model for battery cells and a flow network model. The results of the CFD model was validated with available experimental results (heat transfer and pressure drop) for in-line tube-bank systems which approximates the in-line arrangement of the battery cells considered for this study. The numerical results showed that the shorter the reciprocating period is, the lower the cell temperature difference and the maximum cell temperature (of both instantaneous and time-averaged) of the system. It was shown from the numerical results that the reciprocating flow using a reciprocation period τ = 120 s reduces the cell temperature difference by about 4.0 °C (72% reduction) and the maximum cell temperature by 1.5 °C as compared with the uni-directional case ($\tau = \infty$). The improvement by the reciprocating flow mainly attributes to the heat redistribution and disturbance of the boundary layers formed on the cells due to the periodic flow reversal. The results from the lumped-capacitance thermal model and flow network model were in good agreement with the 2D CFD results. Although the multi-dimensional CFD modeling is essential for the analysis of complex battery systems, time-efficient lumped-capacitance models using appropriate heat transfer correlations would be very suitable for the intensive computations such as battery lifetime prediction based on battery duty cycles and real-time battery temperature forecast and control.

References

[1] C.-W. Park, A.K. Jaura, Reciprocating Battery Cooling for Hybrid and Fuel Cell Vehicles, IMECE 2003-41201.
[2] C.-W. Park, A.K. Jaura, Dynamic Thermal Model of Li-ion Battery for Predictive Behavior in Hybrid and Fuel Cell Vehicles, SAE 2003-01-2286.
[3] C.-W. Park, A.K. Jaura, Transient Heat Transfer of 42 V Ni-MH Batteries for an HEV Application, SAE 2002-01-1964.
[4] A.A. Pesaran, A. Vlahinos, S.D. Burch, Thermal performance of EV and HEV battery modules and packs, in: Proceedings of the 14th International Electric Vehicles Symposium, Orlando, Florida, 15–17 December, 1997, pp. 15–17.

[5] C.G. Motloch, J.P. Christopheresen, J.R. Belt, R.B. Wright, G.L. Hunt, R.A. Sutula, T. Duong, T.J. Tartamella, H.J. Haskins, T.J. Miller, High-Power Battery Testing Procedures and Analytical Methodologies for HEV's, SAE 2002-01-1950.
[6] C.-W. Park, A.K. Jaura, Battery System for Automotive Vehicle, US Patent 7172831B2.
[7] C.-W. Park, M. Kaviany, ASME J. Heat Transf. 124 (2002) 184–194.
[8] K. Hanamura, R. Echigo, S.A. Zhdanok, J. Heat Mass Transf. 36 (1993) 3201–3209.
[9] C.-W. Park, M. Kaviany, ASME J. Heat Transf. 122 (2000) 721–729.
[10] M. Kaviany, Principles of Heat Transfer, first ed., John Wiley & Sons, Inc., New York, 2002.
[11] V. Srinivasan, C.Y. Wang, J. Electrochem. Soc. 150 (2003) A98–A106.
[12] S. Al-Hallaj, R. Venkatachalapathy, J. Prakash, J.R. Selman, J. Electrochem. Soc. 147 (2000) 2432–2436.
[13] K.E. Thomas, C. Bogatu, J. Newman, J. Electrochem. Soc. 148 (2001) A570–A575.
[14] K. Smith, C.-Y. Wang, J. Power Sources 160 (2006) 662–673.
[15] K. Smith, C.-Y. Wang, J. Power Sources 161 (2006) 628–639.
[16] A. Zukauskas, R. Ulinskas, Heat Transfer in Tube Banks in Crossflow, first ed., Hemisphere Publishing, New York, 1988, pp. 63–93.
[17] E.S. Gaddis, V. Gnielinski, Int. Chem. Eng. 25 (1985) 1–15.
[18] A. Zukauskas, Convective heat transfer in cross flow, in: S. Kakac, R.K. Shah, W. Aung (Eds.), Handbook of Single Phase Convective Heat Transfer, Wiley Interscience, New York, 1987.
[19] A. Zukauskas, R. Ulinskas, Heat Transf. Eng. 6 (1985) 19–25.
[20] S. Whitaker, AICHE J. 18 (1972) 361–371.
[21] F.P Incropera, D.P. Dewitt, T.L. Bergman, A.S. Lavine, Introduction to Heat Transfer, fifth ed., John Wiley & Sons, Hoboken, 2007.
[22] D. Linden, Handbook of Batteries, second ed., McGraw-Hill, New York, 1994.
[23] T.I. Evans, R.E. White, J. Electrochem. Soc. 136 (1989) 2145–2152.
[24] ANSYS FLUENT, version 12.1.4, ANSYS Inc., Lebanon, New Hampshire, 2010.
[25] S.V. Patankar, Numerical Heat Transfer and Fluid Flow, first ed., McGraw-Hill, New York, 1980.
[26] GAMBIT, version 2.4.6, Fluent Inc., Lebanon, New Hampshire, 2005.
[27] B. Carnahan, H.A. Luther, J.O. Wilkes, Applied Numerical Methods, first ed., John Wiley & Sons, New York, 1990.
[28] W.A. Khan, J.R. Culham, M.M. Yovanovich, J. Heat Mass Transf. 49 (2006) 4831–4838.